

# Levitation Performance Of Two Opposed Permanent Magnet Pole-Pair Separated Conical Bearingless Motors

Peter Kascak, Ralph Jansen, Timothy Dever  
NASA Glenn Research Center  
Cleveland, USA  
peter.e.kascak@nasa.gov

Aleksandr Nagorny  
ResMed Motor Technologies Inc.  
Los Angeles, USA

Kenneth Loparo  
Case Western Reserve University  
Cleveland, USA

**Abstract—** In standard motor applications, rotor suspension with traditional mechanical bearings represents the most economical solution. However, in certain high performance applications, rotor suspension without contacting bearings is either required or highly beneficial. Examples include applications requiring very high speed or extreme environment operation, or with limited access for maintenance. This paper expands upon a novel bearingless motor concept, in which two motors with opposing conical air-gaps are used to achieve full five-axis levitation and rotation of the rotor. Force in this motor is created by deliberately leaving the motor's pole-pairs unconnected, which allows the creation of different d-axis flux in each pole pair. This flux imbalance is used to create lateral force. This approach is different than previous bearingless motor designs, which require separate windings for levitation and rotation. This paper examines the predicted and achieved suspension performance of a fully levitated prototype bearingless system.

## I. INTRODUCTION

Traditionally motor rotors are suspended from their stators with mechanical bearings. Mechanical bearings provide a very stable platform separating the rotating and stationary parts with relatively very little friction at a very small cost. In most applications this is the preferred solution; these bearings perform over an adequate lifetime, can be readily lubricated, and if necessary easily replaced.

However there are a growing number of high performance applications where the use of mechanical bearings is either unsatisfactory or impossible. These

applications have one or more of the following attributes: extremely fast rotating speed, the need for almost no friction, limited or non-existent opportunity for maintenance, and operation in an extreme environment. Since these applications are very high performance, a higher cost rotor suspension system can be justified.

Magnetic bearings have been used to provide higher performance rotor suspension. Separate magnetic actuators are designed which sense the position of the rotor and apply an appropriate magnetic force to stabilize the position of the rotor. This allows for contact free suspension of the rotor with very little friction, no need for a lubrication system, and no need for maintenance.

One potential drawback of this method is that it adds iron and copper parts dedicated only to the function of rotor levitation, while also requiring the motor to contain iron and copper parts dedicated to only rotation. In addition to increasing parts count, this approach can also increase the axial length of the rotor, which lowers the bending mode frequencies and complicates suspension control at high speeds. Additionally, this separation of functions of the two actuators means that the motor must be sized for the largest torque load the machine will encounter, and the magnetic bearing system must be sized for the largest lateral force necessary to suspend the rotor.

For these reasons it was desired to develop a single actuator, i.e. a bearingless motor; which could produce lateral forces for rotor suspension in addition to the torque

controlling the rotation of the rotor. Bearingless motors were demonstrated in synchronous reluctance [1], [2], induction [3], permanent magnet [4], and switched reluctance [5] motor types. These motors have a common iron structures carrying both levitation and rotation flux. However, they all use different windings for levitation and rotation, which means each function is still limited by windings and power electronics dedicated to a single function. A further limitation is that they are only capable of providing levitation forces in a radial plane in the case of radial motors, or in the axial direction for axial motors.

This paper examines the performance of a new bearingless motor concept, which was previously documented by the authors of this paper in [6]-[11]. Using this new approach the motor pole-pairs are separated, causing a flux imbalance which creates a levitation force. This allows all of the motor iron and copper to be used for either levitation or rotation. Additionally, these motors employ a conical shaped air-gap, enabling creation of axial as well as radial forces. A prototype controller and motor were built, using pair of these motors with opposing cones, and full 5-axis levitation was demonstrated.

The contribution of this paper over [6]-[11] is that it focuses on the suspension performance of the machine, where the previous literature was focused on presenting the basic concept. Furthermore, this paper introduces new parameters which are not commonly measured on electric machines, along with the experimental methods used to measure them. These new parameters are figures of merit on magnetic bearing systems.

## II. SELF LEVITATION BY TWO POLE-PAIR SEPARATED CONICAL MOTORS

### A. Separate control of pole-pairs

Standard electric machines are wound with pole-pairs connected either in series or parallel; series connected windings are shown in Figure 1. These windings do not allow independent control of the flux in each pole-pair separately; the flux of every pole-pair can only be increased or decreased together. For electric machines with rotors suspended using conventional mechanical bearings there is no reason to control the flux in each pole-pair individually; in fact, it is desired that each pole-pair carry the same flux, so as not to induce unwanted vibration.

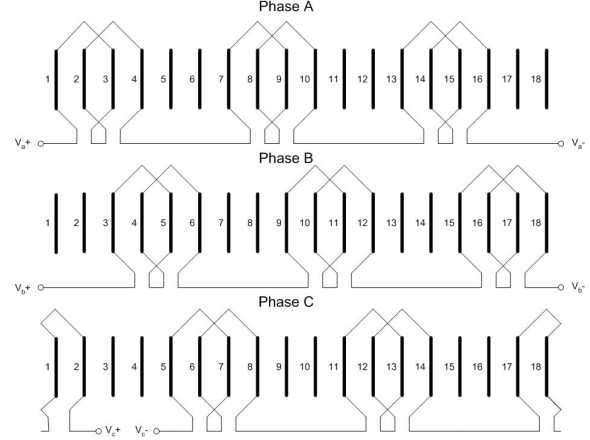


Figure 1: Pole-pairs Connected in Series

The bearingless machine studied in this paper utilizes unconnected pole-pairs, as seen in Figure 2. This configuration allows the flux in each individual pole pair to be varied, allowing a net force to be created on the rotor.

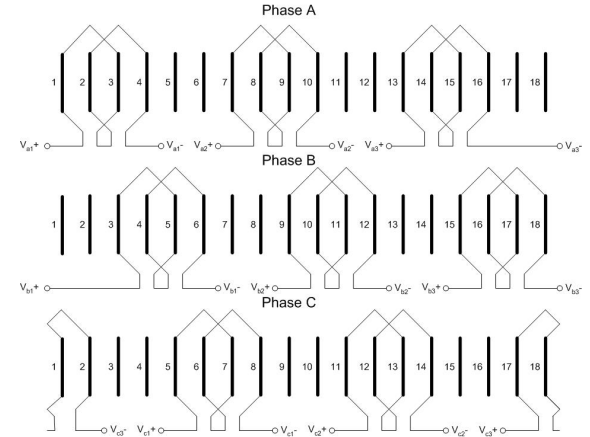


Figure 2: Independent Pole-pair Windings

The electronics needed to drive a standard motor are shown in Figure 3. The pole-pairs are connected in series, and the motor can be controlled with three currents, which requires six switches.

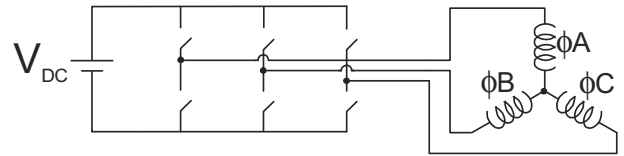


Figure 3: Standard Motor Drive Electronics

More complex electronics are needed to drive the bearingless motor, as shown in Figure 4. Because the pole-pairs are now separate, nine currents have to be controlled. This control requires eighteen switches.

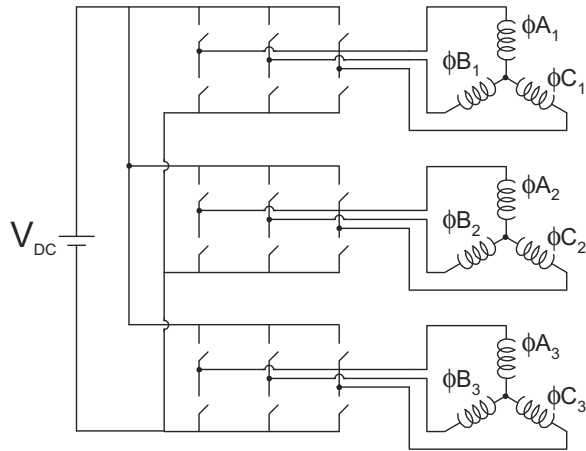


Figure 4: Bearingless Motor Drive Electronics

The higher complexity of the bearingless motor's drive electronics is not necessarily a disadvantage, and in some cases it may prove beneficial. For example, the bearingless drive will require the same silicon area as the standard drive, since the power rating of each switch is one third that of the standard motor. For high power applications, this could be used to eliminate the need to parallel switches, simplifying the system. Additionally, the bearingless drive offers fault tolerant capabilities - if a fault occurs in one of the pole-pairs, operation could continue using the other two pole-pairs.

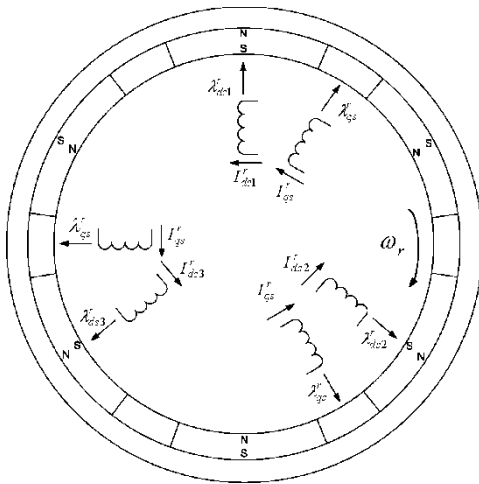


Figure 5: Pole-pairs in the rotor reference frame

The windings of the bearingless motor can be represented in the rotor reference frame; Figure 5 shows the fictional d and q axis windings rotating with the rotor. There are two types of forces which can be created with these windings: the first is the Lorentz force, which is the force associated with the production of torque, and the second is the Maxwell force, which acts in such a way as to minimize the reluctance of the magnetic circuit. The permanent magnet machine studied in this paper was intended for high speed operation; as such the Lorentz forces are much smaller than the Maxwell forces.

The controller sets the q-axis currents equal in each pole-pair; this causes the net force induced by Lorentz type forces to be equal to zero. The d-axis currents in each pole-pair are set to be unequal, which creates a net Maxwell type force. The flux density plot in Figure 6, which was generated using finite element analysis, demonstrates this imbalance. In this test case a large d-axis current is present in one of the pole-pairs, while the other pole-pairs have zero d-axis current.

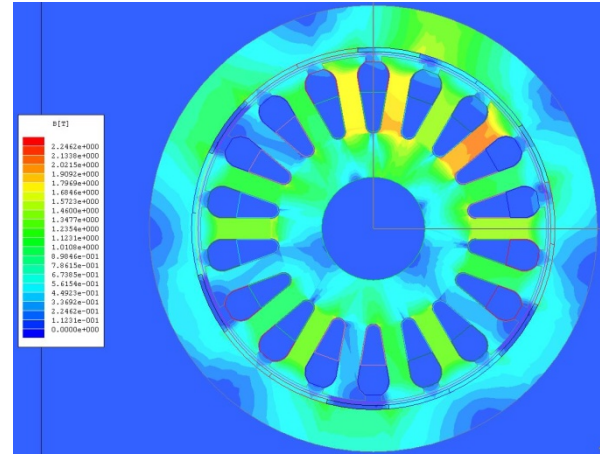


Figure 6: Flux Imbalance due to d-axis current imbalance

#### B. Axial Force Creation with Conical Air-Gap Motors

The Maxwell forces are directed straight across the air-gap; this means that a radial electric machine with a cylindrical air-gap can create only radial forces. In order to fully suspend the rotor it is necessary to control 5-axes, which requires two planes of radial control in addition to axial control. Two cylindrical air-gap motors can't actively control axial force.

In order to allow the active creation of axial forces, the machine studied in this paper employs a conical shaped air-gap. Two motors of this type are arranged such that their cones are oriented in opposite directions; this is shown in Figure 7. In this configuration the forces created by d-axis flux are not purely radial, and have an axial component: the magnitude of the generated force is the same, but the axial component is determined by the cone angle.

Figure 8 shows the forces created by the two motors (note that no attempt has been made in this diagram to show these forces in scale with the actual cone angle). The net axial force is proportional to the difference of the sum of the d-axis currents in the top motor and the sum of the d-axis currents in the bottom motor.

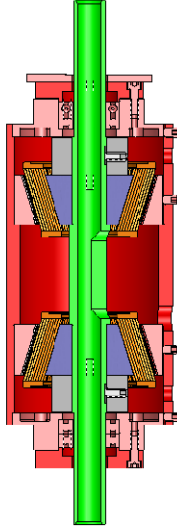


Figure 7: Prototype Machine with two opposed conical motors

### III. PROTOTYPE MACHINE

The motor was sized for a flywheel application with a full speed of 100 kRPM. In order to keep material and construction costs down, a low speed prototype of this motor was constructed to be used to prove the concept of combined levitation and rotation. The low speed requirement allowed the rotor and stator back iron of the machine to be constructed from solid M19 silicon steel. The windings were designed as if this machine would run at full speed in a flywheel application, and produce a back-emf of 110V at 100 kRPM.

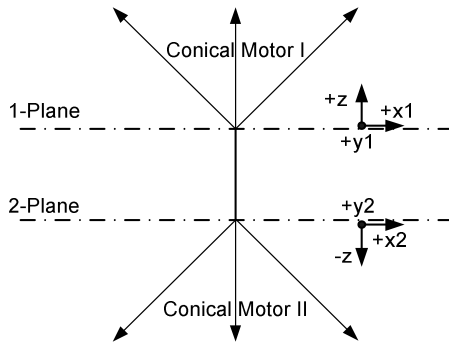


Figure 8: Available Force Vectors

A summary of the motor design described in this paper is provided in Table 1. All of the parameters shown were experimentally confirmed.

Table 1: Prototype Conical Bearingless Motor

Parameter	Design Value
Soft Magnetic Material	M19 Silicon Steel
Permanent Magnets	NdFe30

Poles	6
Turns/coil	10
Number of slots	18
Inner stator diameter	.625 in
Outer stator diameter (mid-point axially)	2.123 in
Inner rotor diameter (mid-point axially)	2.148 in
Outer rotor diameter	2.7 in
Magnet thickness	0.025 in
Mechanical air gap	0.025 in
Slot depth	0.4 in
Axial stack length	1.00 in
Rotor yoke thickness (mid-point axially)	0.2420 in
Stator back iron thickness (mid-point axially)	.3455 in
Slot pitch (tooth and slot)	0.3706 in
Tooth width at air gap	0.2597 in
Mutual Flux Linkage due to rotor flux ( $\lambda_{af}$ )	3.4 mWb-t
q-axis inductance ( $L_q$ )	108 $\mu$ H
d-axis inductance ( $L_d$ )	81 $\mu$ H

### IV. SIMULATION MODELS

This paper employs three different models to obtain simulation results: a magnetic circuit model, a finite element model, and a control system model.

#### A. Magnetic Circuit Model

A magnetic circuit model was used to design and analyze the conical bearingless motor presented in this paper. In this model flux is assumed to travel straight through magnetic circuit elements; these can also be thought of as flux tubes. A magnetic circuit model can be created with as many elements as are necessary to accurately represent the device which they model; of course, the more elements that are used, the longer and more computationally intensive the simulation becomes. The conical motor has dimensions which vary axially; however, for this analysis the average dimensions of the motor are used to simplify the analysis. The model used for analysis of this motor is shown in Figure 9.

This model is solved by expressing 36 loop equations, 18 stator loops and 18 rotor loops. Because the reluctance of the iron parts is a function of the flux which passes through them, this model is solved iteratively. The coils are represented by the "tooth" MMFs; the iron parts and the permanent magnets are represented by an MMF source and a series reluctance; and the air gap and leakage are represented by a simple reluctance.

First, an initial value of flux is first assumed for each loop flux. Next, using the model, the MMF source and series reluctance of each iron element is calculated at these

flux levels. Then the loop equations are solved, and new flux values are obtained. The process is repeated until the difference between new and previous flux values converges to an appropriate tolerance.

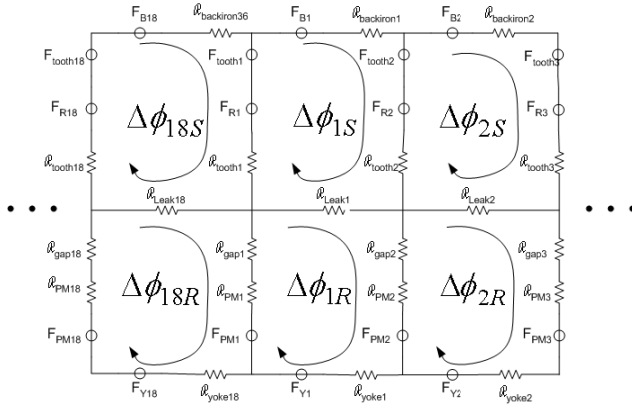


Figure 9: Magnetic Circuit Model

### B. Finite Element Model

A finite element model was also employed to analyze this motor. A 2-d magnetostatic model was used. Because the conical shaped motor has dimensions which vary axially, the plane in the middle of the motor was used for this analysis.

The finite element model does not use the simplifying assumptions of the magnetic circuit model; it solves for the actual field solution. It is more accurate than the magnetic circuit model; however, it takes much longer to run cases. Additionally, relying only on this type of model can result in the loss of valuable design insight. For these reasons the finite element model was used to verify and fine tune the design obtained by magnetic circuit modeling.

### C. Control System Model

In addition to the magnetics models, a control system model was created in MATLAB/Simulink. This model is of the entire controller and plant, including: a dynamic model of rotor mechanics, inverter delay, both bearingless motors, and the controller (run at 0.3 ms sample time).

## V. RESULTS

### A. Levitation and Rotation

The prototype motor was successfully levitated and spun at a variety of speeds. Rotor position is measured and fed to the controller using non-contact eddy current sensors, which measured x and y radial positions at the top and bottom of the machine, and axial position.

During 300 RPM operation, data was taken on the motor currents and the rotor position in 5 axes. The x-y plots of the top and bottom radial positions during operation are presented in Figure 10 and Figure 11, and the axial position during operation is shown in Figure 12.

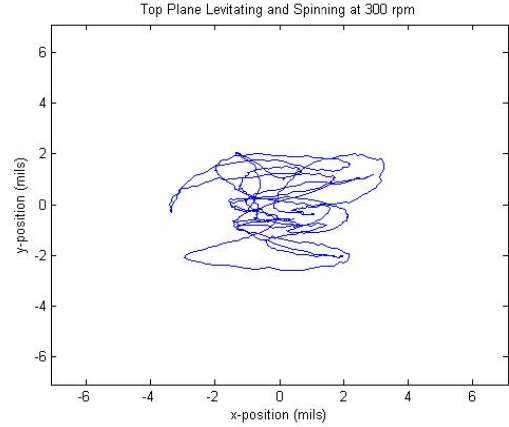


Figure 10: x and y position measured by top sensor plane, levitating and spinning at 300 RPM

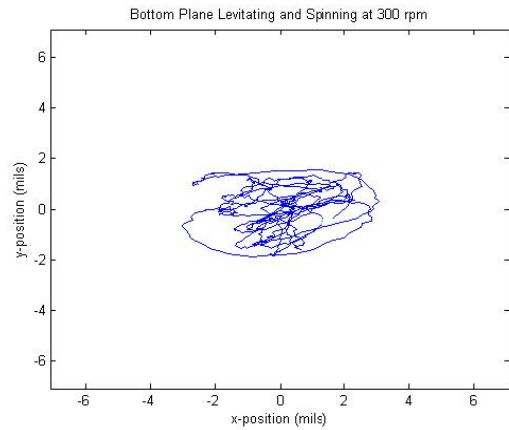


Figure 11: x and y position measured by bottom sensor plane, levitation and spinning at 300 RPM

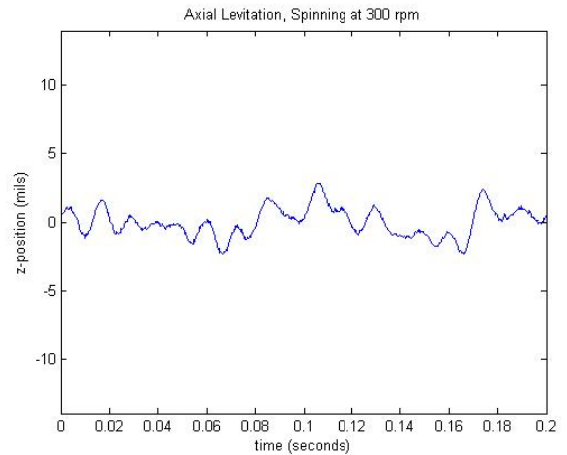


Figure 12: Rotor axial position, levitating and spinning at 300 RPM

### B. Stability

Next, the loop gain of the bottom plane x controller was measured in hardware, and compared to the loop gain obtained through simulation. The comparison is shown in



Figure 13. Note that the measured loop gain matches the simulated loop gain fairly well, except for around 32.5 Hz.

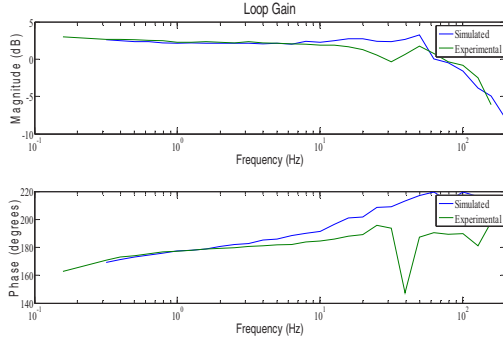


Figure 13: Open loop transfer function of PID position control loop

To try to understand the origin of the extra mode seen in the experimental data, a standard rap test was performed on the motor. An accelerometer was attached in the center of the mounting plate, and the hammer was struck close by. The results, in Figure 14, show a clear dip in magnitude at 32.5 Hz which is consistent with the experimental loop gain data. Based on the rap test results, it was concluded that the extra 32.5 Hz mechanical mode was likely a rigid body mode of the motor baseplate interacting with the mounting isolation dampers.

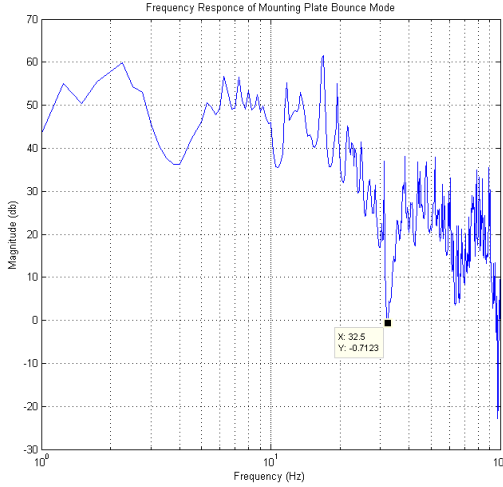


Figure 14: Rap test

Finally, the experimental loop gain data was used to generate a transfer function, which represents the open loop system, and is useful in stability analysis.

First, the experimental loop gain data was fit to a ratio of complex polynomials [12], [13]. Since the controller has a known sample time of 0.3 ms, this delay was divided out of the loop gain data, then the delay free data was curve fit. This process yields the following:

$$T(s) = T_{no-delay}(s) \cdot e^{-s \cdot 3e-3} \quad (1)$$

$$T_{no-delay}(s) = \frac{N_{no-delay}(s)}{D_{no-delay}(s)} \quad (2)$$

$$N_{no-delay}(s) = -6.06 \cdot 10^{-11} \cdot s^5 + 5.12 \cdot 10^{-8} \cdot s^4 + 1.88 \cdot 10^{-5} \cdot s^3 + 2.28 \cdot 10^{-3} \cdot s^2 + 1.31 \cdot s + .392 \quad (3)$$

$$D_{no-delay}(s) = 2.37 \cdot 10^{-14} \cdot s^6 + 1.32 \cdot 10^{-10} \cdot s^5 - 1.41 \cdot 10^{-8} \cdot s^4 - 7.60 \cdot 10^{-6} \cdot s^3 - 5.22 \cdot 10^{-5} \cdot s^2 - s \quad (4)$$

Using (3) and (4), the zeros and poles of the open loop transfer function were calculated. The transfer function has the following zeros:

$$s = 1160, -333, 11.1 \pm j237, -0.3 \quad (5)$$

And the following poles:

$$s = 0, -5650, 378, -320, 18.6 \pm j248 \quad (6)$$

Also using (3) and (4), a Nyquist stability plot was generated, and is shown in Figure 15. Although the open loop transfer function has three poles in the right hand plane, the Nyquist stability plot shows that -1 is encircled three times in the counter clockwise direction, which guarantees that the closed loop system is stable.

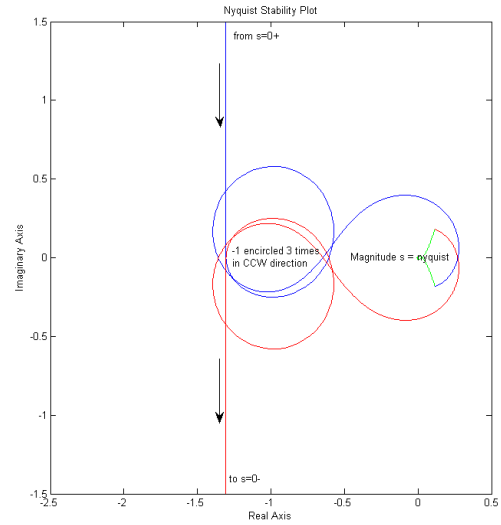


Figure 15: Nyquist stability plot of PID position control loop

### C. Levitation Parameters

Now the suspension capabilities of the bearingless machine are examined. The two parameters of interest are the *current stiffness* and the *negative position stiffness* of the bearingless machine.

The current stiffness is the amount of force created for every amp of levitation current. To measure this, a known

force is applied in the radial direction to one of the conical motors; this is done by hanging a known weight from a pulley and attaching it to the center of the rotor, seen in Figure 16.



Figure 16: Force Applied to Bearingless Machine

In order to determine the current stiffness from this test it is necessary to determine the current effort required to maintain levitation. This can be achieved by adding the d-axis current in each pole-pair vectorially. Note the forces created by each pole-pair are in directions that are separated by 120 degrees from each other; this allows current effort of each pole-pair to be expressed as vectors:

$$\vec{i}_{d11}^r = i_{d11}^r \quad (7)$$

$$\vec{i}_{d12}^r = i_{d12}^r \cdot \vec{a} \quad (8)$$

$$\vec{i}_{d13}^r = i_{d13}^r \cdot \vec{a}^2 \quad (9)$$

Where  $\vec{a} = e^{i \cdot 120^\circ}$  and  $i_{d11}^r, i_{d12}^r, i_{d13}^r$  are the d-axis current of each pole-pair in the first motor. Now the total levitation current effort can be expressed as:

$$I_{effort} = |\vec{i}_{d11}^r + \vec{i}_{d12}^r + \vec{i}_{d13}^r| \quad (10)$$

The current stiffness can now be expressed as:

$$k_{current} = \frac{F_{weight}}{I_{effort-weight} - I_{effort-noweight}} \quad (11)$$

Where  $F_{weight}$  is the force applied by the weight,  $I_{effort-weight}$  is the current effort required for levitation with the applied force, and  $I_{effort-noweight}$  is the current effort required to levitate the rotor with no applied force.

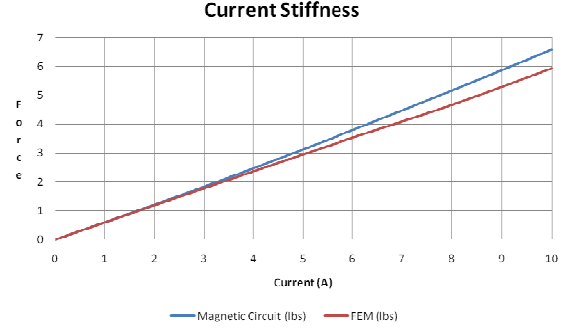


Figure 17: Current Stiffness (Magnetic Circuit and Finite Element Models)

Using the above approach, the current stiffness was measured with several different applied weights. The average value of current stiffness was found to be 0.59 lbs/A. Current stiffness was also determined using both the magnetic circuit and finite element models; this was done by applying d-axis current to a pole-pair and noting the magnitude of the resulting force. Figure 17 shows force versus current for both simulation models; the slope of the line is the current stiffness. Table 2 summarizes the current stiffness obtained by the two models, and experimentally. Note the excellent agreement between all three approaches.

Table 2: Current Stiffness

	Current Stiffness
Magnetic Circuit	0.60 lbs/A
Finite Element	0.59 lbs/A
Experimental	0.59 lbs /A

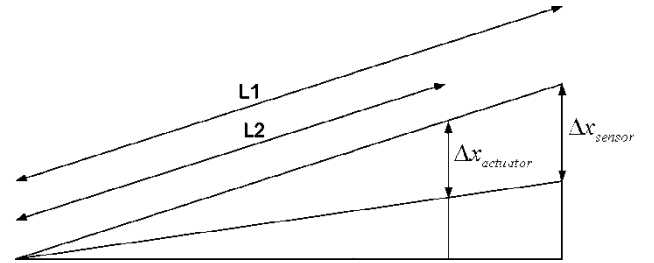


Figure 18: Lever arms to motor and sensor plane

Next, the negative position stiffness is addressed. The negative position stiffness is the amount of force created on the rotor by moving it off of the magnetic center. Since the current stiffness is known, the force created by moving the rotor off center can be calculated as:

$$F_{position} = (I_{effort-offcenter} - I_{effort-center}) \cdot k_{current} \quad (12)$$

The position stiffness is then simply:

$$k_{position} = \frac{F_{position}}{\sqrt{\Delta x^2 + \Delta y^2}} \quad (13)$$

Where

$$\Delta x = x_{offcenter-act} - x_{center-act} \quad (14)$$

$$\Delta y = y_{offcenter-act} - y_{center-act} \quad (15)$$

Therefore the negative position stiffness can be measured by levitating the rotor, observing the current effort, then moving the rotor off center and observing the new current effort. There are two motors in this system; for this measurement we refer to them as the motor under test (MUT) and the motor not under test (MNUT). During the measurement the MNUT is levitated, holding its position centered at its sensor plane.

It is important to note that the above equations refer to movement at the center of the MUT, which is not coplanar with the sensors. Figure 18 shows the geometry of this measurement; the left most point of the triangle is the sensor plane of the MNUT. L2 is the distance from that sensor plane to the center of the MUT; L1 is the distance between the sensor planes of both motors. Movement of the rotor observed in the sensor plane can be expressed in its motor center plane as:

$$\Delta x = \frac{L2}{L1} \cdot \Delta x_{sensor} \quad (16)$$

The above measurement was performed on both the top and bottom motors, using various displacement values. The average measured negative position stiffness for both motors over the displacement range was 860 lbs/in. The negative position stiffness was also determined using simulation by moving the rotor off center and observing the net force; simulations were performed using both models. Figure 19 shows force versus rotor displacement for both the magnetic circuit model and the finite element model; the negative stiffness is the slope of these lines. A summary of the negative position stiffness using both simulation methods and experimental results is presented in Table 3. Note the close agreement between all three approaches.

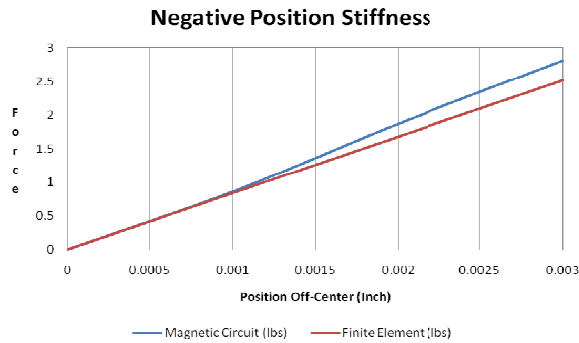


Figure 19: Negative Position Stiffness (Magnetic Circuit and Finite Element Models)

Table 3: Negative Position Stiffness

	Negative Position Stiffness
--	-----------------------------

Magnetic Circuit	862 lbs/in
Finite Element	842 lbs/in
Experimental	860 lbs/in

## VI. CONCLUSION

This paper expands upon the conical bearingless concepts put forward previously by the authors. First, the basic concepts of the bearingless motor are briefly presented. Next the fully levitated, two-motor prototype rig is described. Three methods of simulation are described, including their specific uses. Following this results are presented: position control while rotating, stability analysis, and levitation performance of the prototype machine. Experimental results closely match those obtained in simulation. The main contribution of this paper is in examining the bearingless motor's performance as a rotor suspension system.

## REFERENCES

- [1] A. Chiba, K. Chida and T. Fukao, "Principles and Characteristics of a Reluctance Motor with Windings of Magnetic Bearing", in *Proceedings of International Power Electronic Conference (IPEC-Tokyo)*, 1990, pp. 919-926.
- [2] A. Chiba, M. A. Rahman and T. Fukao, "Radial Force in a Bearingless Reluctance Motor", *IEEE Transactions on Magnetics*, Volume 27, Issue 2, pp. 786-790, March 1991. K. Elissa, "Title of paper if known," unpublished.
- [3] A. Chiba, D. T. Power, M. A. Rahman, "No Load Characteristics of a Bearingless Induction Motor", *IEEE Transactions on Magnetics*, Volume 27, Issue 6, pp. 5199-5201, November 1991.
- [4] K. Dejima, T. Ohishi, and Y. Okada, "Analysis and control of a permanent magnet type levitated rotating motor," in *IEEEJ Proceedings of Symposium Dynamics of Electro Magnetic Force*, June 1992, pp. 251-256.
- [5] K. Shimada, M. Takemoto, A. Chiba, and T. Fukao, "A Stable Rotation in Switched Reluctance Type Bearingless Motors", in *Papers of IEEEJ Technical Meeting on Linear Drive*, 1997, LD-97-116.
- [6] P. Kascak, "Fully Levitated Rotor Magnetically Suspended by Two Pole-Pair Separated Conical Motors," Ph.D. Thesis, Case Western Reserve University, Cleveland, OH, 2010.
- [7] P. Kascak, R. Jansen, and T. Dever, "Control System for Bearingless Motor-Generator", U.S. Patent 7,456,537 B1, Nov. 25, 2008.
- [8] P. Kascak, R. Jansen, and T. Dever, "Control System for Bearingless Motor-Generator", U.S. Patent 7,667,418, Feb. 23, 2010.
- [9] P. Kascak, R. Jansen, T. Dever, A. Nagorny, and K. Loparo, "Bearingless Five-Axis Rotor Levitation with Two Pole Pair Separated Conical Motors", in the *Conference Record of IEEE Industrial Applications Society Annual Meeting*, October 2009.
- [10] P. Kascak, T. Dever, R. Jansen, "Conical bearingless motor-generators", in *McGraw-Hill Yearbook of Science & Technology*, 2010 edition, pp. 81-84.
- [11] P. Kascak, T. Dever, R. Jansen, A. Nagorny, and K. Loparo, "Motoring Performance of a Conical Pole-Pair Separated Bearingless Electric Machine", in the *Conference Record of IEEE EnergyTech*, May 2011.
- [12] E. C. Levy, "Complex-Curve Fitting," in *IRE transactions on automatic control*, pp. 37-44, 1959.
- [13] C. K. Sanathanan and J. Koerner, "Transfer Function Synthesis as a Ratio of Two Complex Polynomials," in *IEEE Transactions on Automatic Control*, vol. 8, issue 1, pp. 56-58, January, 1963.